Influence of the Mg-content on the cation distribution in cubic $Mg_xFe_{3-x}O_4$ nanoparticles

F. Nakagomi [a,*], S.W. da Silva [a], V.K. Garg [a], A.C. Oliveira [a], P.C. Morais [a], A. Franco Jr. [b]

[a] Universidade de Brasília, Instituto de Física, Núcleo de Física Aplicada, Brasília, DF 70910-900, Brazil
[b] Universidade Federal de Goiás, Instituto de Física, Goiânia, GO 74001-970, Brazil

ARTICLE INFO

ABSTRACT

The influence of the Mg-content on the structural and magnetic properties of cubic $Mg_xFe_{3-x}O_4$ nanoparticles prepared by combustion reaction was investigated using X-ray diffraction, transmission electron microscopy (TEM), Mössbauer spectroscopy, and Raman spectroscopy. Lattice parameter, nanoparticle size, and cation (Mg^{2+}, Fe^{3+}) distribution were quantified as a function of the Mg-content in the range $0.5 \leq x \leq 1.5$. We found a mixed-like spinel structure at the smaller x-value end whereas the inverse-like spinel structure dominates samples with larger x-values. Moreover, in the x-value range investigated ($0.5 \leq x \leq 1.5$) we found no change in the quadrupole splitting and isomer shift values, though the hyperfine field decreases as the x-value increases. The splitting of the A_{1g} Raman mode was used to both quantify the Mg^{2+}/Fe^{3+} contents in the tetrahedral site and obtain the cation distribution in the $Mg_xFe_{3-x}O_4$ structure. The cation distribution obtained from the Raman data is in very good agreement with the cation distribution obtained from the Mössbauer data.

© 2009 Elsevier Inc. All rights reserved.

1. Introduction

The most remarkable effect in spinel ferrites is the strong dependence of physical properties on cation composition and structural ordering, in particular the dependence on the metal distribution among the two available interstitial sites. The spinel structure presents two types of interstitial sites, namely tetrahedral (A) and octahedral (B) surrounded by four and six oxygen atoms, respectively. The general formula of spinel ferrites is MB_2O_4, where M occupies the tetrahedral site whereas B occupies the octahedral one. Full occupation of the tetrahedral sites with M^{2+} ions produces the normal spinel structure whereas occupation of the octahedral sites with all M^{2+} ions produces the inverse spinel structure. Mixed or disordered spinel structure presents M^{2+} ions occupying both A- and B-sites. Magnetite (Fe_3O_4) for instance presents the inverse spinel structure, in which Fe^{2+} ions occupy the octahedral (B) sites and Fe^{3+} ions occupy equally both the tetrahedral and the octahedral sites, herein described by the chemical formula $(Fe^{3+})_A(Fe^{2+}Fe^{3+})_BO_4$. The Fe^{2+} ions can be increasingly replaced by divalent metal ions (e.g. Mg, Co, Zn, and Mn), leading to the empirical formula $Mg_xFe_{3-x}O_4$. In fact, most of the cubic ferrite properties strongly depend on the cation distribution among the tetrahedral and octahedral sites as well as on the particular

divalent metals employed. For instance, cobalt ferrite ($CoFe_2O_4$) is a hard magnetic material presenting high chemical stability and notable physical properties such as large magnetic anisotropy and high magnetic coercivity values [1]. On the other hand magnesium ferrite ($MgFe_2O_4$) is a soft magnetic material that presents important photoelectric properties [2,3], addressing a number of applications in heterogeneous catalysis, adsorption, sensors, and in magnetic technologies [4–6].

Mössbauer spectroscopy has been widely used to accurately determine the M^{2+}-site occupancy in spinel ferrites. However, for quaternaries such as $Zn_xMg_{1-x}Fe_2O_4$, Mössbauer measurements alone cannot determine the Zn and Mg distribution due to the limitation of the Mössbauer spectroscopy in probing only iron. It is well known, however, that localized vibrational mode absorption is directly proportional to the substitutional impurity concentration. Using Raman spectroscopy Seong et al. [7] compared the N concentration in $GaAs_{1-x}N$ (x_{Raman}) with the values determined using X-ray diffraction (XRD; x_{XRD}). Similarly to the strategy proposed by Seong et al. [7] Raman and Mössbauer spectroscopies were complementarily used in the present study to investigate a series of the mixed spinel $Mg_xFe_{3-x}O_4$ ($0.5 \leq x \leq 1.5$).

2. Experiments

Nanosized magnesium ferrite ($Mg_xFe_{3-x}O_4$) particles with $0.5 \leq x \leq 1.5$ were synthesized by the combustion reaction method,

* Corresponding author. Fax: +55 61 3307 2363.
E-mail addresses: fabio.nakagomi@gmail.com, nakagomi@unb.br
(F. Nakagomi).

as recently reported in the literature [8]. The chemical composition (total iron and magnesium contents) of all magnesium ferrite samples was determined by atomic absorption spectrophotometry using the commercial Perkin-Elmer 5000 system. The calculated composition is in good agreement with the core chemical composition determined by atomic spectroscopy (see the first two columns of Table 1). The as-prepared powder samples were characterized by room-temperature X-ray diffraction using a Shimadzu diffractometer with Cu K-alpha radiation ($\lambda = 1.5418$ Å) at a scanning rate of 2°/min, in the Bragg's angle range of $15^\circ < 2\theta < 80^\circ$. The average particle diameters were calculated from the XRD line broadening of the (311) reflection using the Scherrer's equation [9]. Transmission electron microscopy (TEM) micrographs were obtained in a Zeiss CEM 902, at an accelerating voltage of 80 kV. For TEM evaluations samples were dispersed in 3 mL of n-propanol and sonicated for 5 min. Droplets of this dispersion were placed over copper grids coated with parlodion and carbon films and dried in air. Liquid-nitrogen-temperature Mössbauer spectra of the as-produced samples were recorded in the transmission geometry using the ^{57}Co source in Rh matrix. The system's velocity was calibrated with a thin iron foil whereas the spectra were least-square fitted to a combination of Lorentzian-like lines. The Raman system used to record the spectra of the samples was a commercial triple spectrometer (Jobin Yvon Model T64000) equipped with a charge-coupled device (CCD) detector. The 514 nm line from an argon-ion laser was used to illuminate the samples at an optical power of around 0.2 mW. All Raman measurements were performed at room temperature.

3. Results and discussions

All nanosized $Mg_xFe_{3-x}O_4$ ($0.5 \leq x \leq 1.5$) samples evaluated in this study were examined by XRD in order to determine the crystal structure, lattice constant, and average particle diameter. Fig. 1 shows the XRD patterns of all synthesized powder samples. From the analysis of the XRD we found that all samples, except for $x = 0.5$ (showing traces of α-Fe_2O_3), are single-phased cubic spinel structures, confirming the reported yielding of the synthesis route used. The analysis of the XRD patterns of the samples revealed an average crystalline diameter slightly depending on the Mg-content (x), ranging from 40 ± 4 nm (for $Mg_{0.5}Fe_{2.5}O_4$) up to 50 ± 4 nm (for $Mg_{1.5}Fe_{1.5}O_4$). The inset of Fig. 1 shows the dependence of the lattice parameter on Mg-content. In the range $0.5 < x < 1.0$, the lattice parameter increases with

increasing Mg-content. However, for $x \geq 1.0$ the lattice parameter stays roughly constant. This finding reveals a deviation from the Vegard's law, which predicts a linear decrease of the lattice parameter with an increase of Mg-content. Deviation from the linear behavior could be explained considering the presence of Mg^{2+} ions in both tetrahedral and octahedral sites [10]. In fact, non-linear behavior has been reported in mixed spinel ferrite systems [11,12].

The diameter values obtained from the XRD data are slightly smaller than the values obtained from the TEM micrographs, the
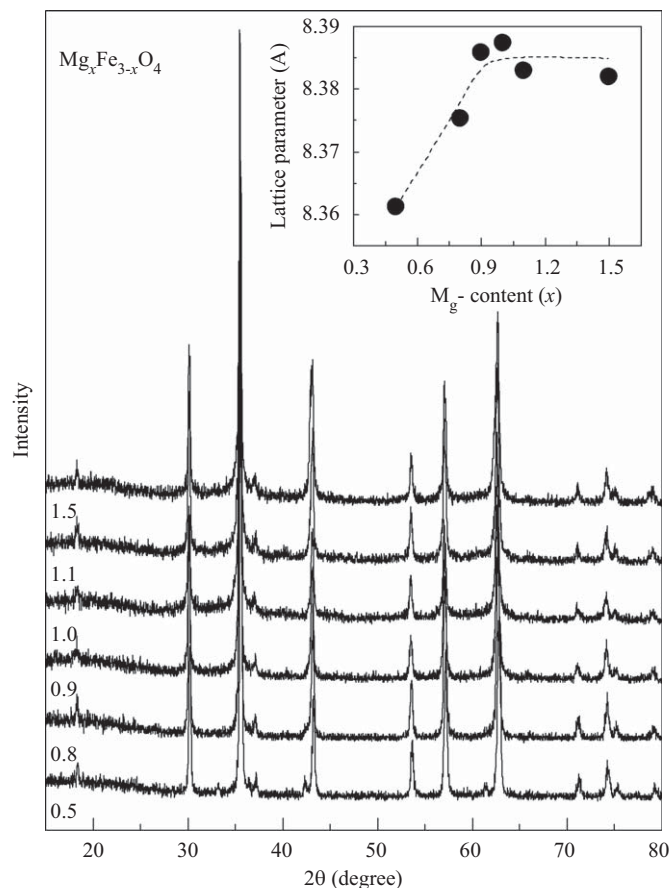

Fig. 1. X-ray diffraction patterns of $Mg_xFe_{3-x}O_4$ ($0.5 \leq x \leq 1.5$) samples. The inset shows the lattice parameter as a function of Mg^{2+}-content.

Table 1

Cation distribution as obtained by Mössbauer (upper row) and Raman spectroscopy (lower row).Magnetic moments calculated by Néel's model and obtained by hysteresis loop measurements in units of Bohr magneton (μ_B). The first two columns show the calculated composition, based on the proportions of the starting materials, and chemical composition determined by atomic spectroscopy.

$Mg_xFe_{(3-x)}O_4$ $x/(3-x)$		Technique	Cations' distribution	Magnetic moments (μ_B)	
Calc.	Exp.			Calc.	Exp.
0.5/2.5	0.47/2.53	Mössbauer	$[Fe^{3+}_{1.00}]_A[Mg^{2+}_{0.47}Fe^{3+}_{1.00}Fe^{2+}_{0.53}]_BO_4$	2.12	2.10
		Raman	$[Fe^{3+}_{0.96}Mg^{2+}_{0.04}]_A[Mg^{2+}_{0.43}Fe^{3+}_{1.08}Fe^{2+}_{0.47}]_BO_4$	2.48	
0.8/2.2	0.82/2.18	Mössbauer	$[Fe^{3+}_{0.89}Mg^{2+}_{0.11}]_A[Mg^{2+}_{0.69}Fe^{3+}_{1.15}Fe^{2+}_{0.14}]_BO_4$	1.86	1.85
		Raman	$[Fe^{3+}_{0.90}Mg^{2+}_{0.10}]_A[Mg^{2+}_{0.72}Fe^{3+}_{1.10}Fe^{2+}_{0.18}]_BO_4$	1.72	
0.9/2.1	0.87/2.13	Mössbauer	$[Fe_{0.89}Mg^{2+}_{0.11}]_A[Mg^{2+}_{0.76}Fe^{3+}_{1.11}Fe^{2+}_{0.13}]_BO_4$	1.62	1.71
		Raman	$[Fe^{3+}_{0.87}Mg^{2+}_{0.13}]_A[Mg^{2+}_{0.74}Fe^{3+}_{1.13}Fe^{2+}_{0.13}]_BO_4$	1.82	
1.0/2.0	1.01/1.99	Mössbauer	$[Fe^{3+}_{0.85}Mg^{2+}_{0.15}]_A[Mg^{2+}_{0.86}Fe^{3+}_{1.14}]_BO_4$	1.40	1.60
		Raman	$[Fe^{3+}_{0.86}Mg^{2+}_{0.14}]_A[Mg^{2+}_{0.87}Fe^{3+}_{1.13}]_BO_4$	1.30	
1.1/1.9	1.08/1.92	Mössbauer	$[Fe^{3+}_{0.80}Mg^{2+}_{0.20}]_A[Mg^{2+}_{0.88}Fe^{3+}_{1.12}]_BO^{2-}_{3.96}\square_{0.04}$	1.60	1.44
		Raman	$[Fe^{3+}_{0.80}Mg^{2+}_{0.20}]_A[Mg^{2+}_{0.88}Fe^{3+}_{1.12}]_BO^{2-}_{3.96}\square_{0.04}$	1.60	
1.5/1.5	1.3/1.70	Mössbauer	$[Fe^{3+}_{0.74}Mg^{2+}_{0.26}]_A[Mg^{2+}_{1.04}Fe^{3+}_{0.96}]_BO^{2-}_{3.96}\square_{0.15}$	1.10	1.19
		Raman	$[Fe^{3+}_{0.75}Mg^{2+}_{0.25}]_A[Mg^{2+}_{1.05}Fe^{3+}_{0.95}]_BO^{2-}_{3.96}\square_{0.15}$	1.00	

latter varying from 45 ± 8 nm (for $Mg_{0.5}Fe_{2.5}O_4$) up to 48 ± 8 nm (for $Mg_{1.5}Fe_{1.5}O_4$). Fig. 2 shows a representative TEM micrograph of sample $MgFe_2O_4$ ($x = 1.0$), revealing powder samples consisting of agglomerates of nanoparticles, roughly spherical in shape.

All synthesized $Mg_xFe_{3-x}O_4$ samples reported in this study were examined by Mössbauer spectroscopy at 77 K, as shown in Fig. 3. The spectra present slightly asymmetric magnetic hyperfine patterns, similar to the one previously observed for $MgFe_2O_4$ [13]. In order to investigate the effect of increasing x-value, all Mössbauer spectra were curve fitted with a combination of
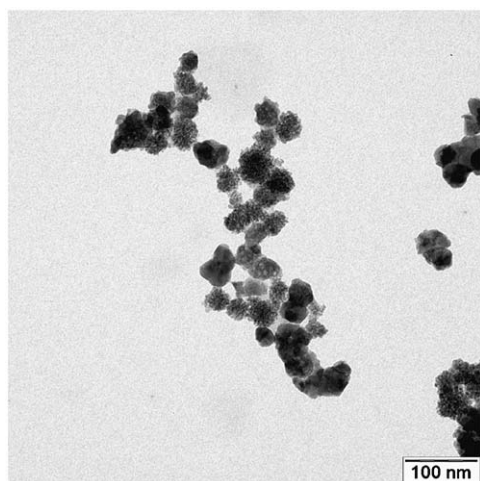

Fig. 2. TEM micrograph of the $MgFe_2O_4$ sample.

sextets. The curve fittings for samples with $x = 0.8$, 1.0, 1.1, and 1.5 were accomplished using two well-defined sextets. Mössbauer spectra of samples with $x = 0.5$ and 0.9 were fitted with three sextets instead. The first and the second sextets were assigned to Fe^{3+} located in tetrahedral and octahedral sites of the cubic spinel structure. In spite of the XRD data showing the presence of a second phase only for $x = 0.5$ the third sextet, though weak, suggested the presence of a second phase also for the $x = 0.9$ sample. Further, an extra doublet was necessary to fit the Mössbauer spectrum of the $x = 1.5$ sample. In principle, this doublet could suggest the presence of a paramagnetic phase. However, Mössbauer spectra recorded at room temperature showed that this effect is associated with the superparamagnetic behavior of the nanoparticles, probably related to the size dispersion in this sample. Taking into account only the data obtained from the curve fitting of the Mössbauer spectra we extracted the values of Mg- and Fe-contents associated with the two sublattices (A and B) and plotted them as function of the Mg substitution, as shown in Figs. 4(a) and (b). The values obtained for the relative Fe-content, hyperfine field (HF), quadruple splitting (QS), and isomer shift (IS) are shown in Figs. 4(c)–(f), respectively.

Data obtained from the analysis of the Mössbauer spectra show that for $x = 0.5$ the Mg-content is entirely associated with the octahedral site (see Fig. 4(a)). However, as x increases the introduced Mg^{2+} ions start to populate both sites, though the occupancy of the octahedral site is more than twice the occupation of the tetrahedral site. The corresponding reduction of the Fe-content in both sites follows the same tendency (see Fig. 4(b)). Fig. 4(c) shows that lower x-values favor mixed spinel structure whereas the increase in Mg-content favors the inverse spinel structure. This behavior is completely different from the
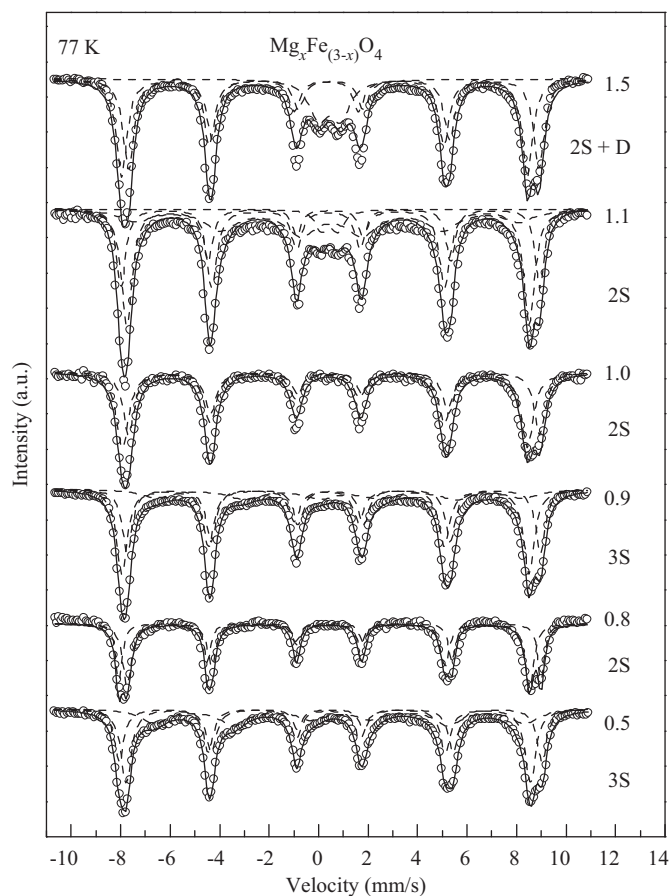

Fig. 3. Mössbauer spectra of $Mg_xFe_{3-x}O_4$ ($0.5 \leq x \leq 1.5$) samples recorded at 77 K.
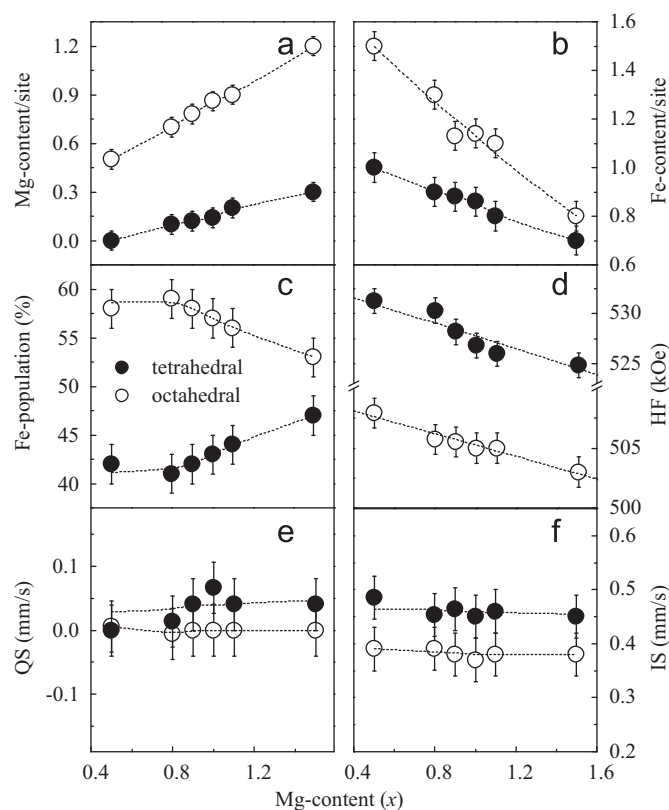

Fig. 4. Magnesium-content dependence of (a) Mg-content per site (A and B), (b) Fe-content per site (A and B), (c) Fe population (%), (d) hyperfine field (HF), (e) quadruple splitting (QS), and (f) isomer shift (IS). The open and solid symbols represent octahedral (B) and tetrahedral (A) sites, respectively. The dashed lines are only guide to the eyes.

behavior observed in the case of Co-substituted ferrite as the Co-content increases [14]. In Co-substituted ferrite the structure changes from the inverse-like to mixed-like spinel structure as the Co-content increases.

Data on Fig. 4(d) show that the HFs associated to both crystallographic sites (A and B) of samples $Mg_xFe_{3-x}O_4$ ($0.5 \leq x \leq 1.5$) decrease monotonically as the Mg-content increases. This finding can be explained using the model introduced by Sawatzky et al. [15], which takes into account the superexchange interaction among the neighboring metal ions in the spinel structure. The model uses the distribution of the metal ions as the nearest neighbors of the Fe ions whereas the molecular field at the Fe-site is described in terms of the exchange integral (J) due to the nearest neighbors. For instance, Fe^{3+} ions on B-sites are surrounded by six nearest O^{2-} ions, each one bounded to the nearest A-sites occupied by metal ions (Fe–O_6–$M_6^{1,2}$, with $M^1 = Mg$ and $M^2 = Fe$). Further, Fe^{3+} ions on A-sites are surrounded by twelve nearest metal ions located on B-sites (Fe–O_4–$M_{12}^{1,2}$, with $M^1 = Mg$ and $M^2 = Fe$). Neglecting B–B interactions and assuming only two types of metal ions on A-sites, labeled as A_1 (Mg) and A_2 (Fe), Sawatzky et al. [15] described the HF on B-sites as

$$H(B) = 2J_1 n \langle S_z(A_1) \rangle + 2J_2(6-n) \langle S_z(A_2) \rangle, \qquad (1)$$

where J_1 and J_2 are the exchange integrals associated to A_1- and A_2-sites, respectively. The number of metal ions occupying A_1-sites was labeled n whereas $(6-n)$ describes the number of ions occupying A_2-sites. $\langle S_z(A_{1,2}) \rangle$ represents the average value of the z-component of the spin associated to the two types of ions referred to as subscripts 1(Mg) and 2(Fe). Once the Mg^{2+} ion has no spin the $Fe^{3+}(B)$–O–$Mg^{2+}(A)$ superexchange interaction is null, and only the second term remains in Eq. (1). Therefore, the HF associated to the B-site will depend only on the Mg-content on the A-site. Then, one should expect the HF on B-site to decrease linearly as the x-value increases, as shown in Fig. 4(d). A similar description applies to the x-dependence of the HF associated to the A-site (see solid symbols in Fig. 4(d)).

In regard to the findings related to both QS and IS, shown in Figs. 4(e) and (f) respectively, one can conclude that changes in the Mg^{2+} ion content in the range of our investigation introduces small changes in the hyperfine parameters of Fe^{3+} ion located on sites A or B. In other words, replacement of Fe by Mg in the spinel $Mg_xFe_{3-x}O_4$, in a wide range of values ($0.5 \leq x \leq 1.5$), introduces small changes in the charge symmetry around sites A and B as well as small changes in the charge density onto Fe^{3+} ions located in both crystallographic sites. These findings are in good agreement with the observations reported for the spinel $Co_xFe_{3-x}O_4$ with $0.6 \leq x \leq 1.6$ [14].

Considering the Mössbauer data presented in Fig. 4(c) and taking into account charge balance requirements it was possible to propose the cation distribution for the synthesized samples. However, in order to select one particular cation distribution profile among different possibilities of cation occupancy, magnetization measurements were performed and the corresponding findings were also considered. Hysteresis loops at 77 K of samples $Mg_xFe_{3-x}O_4$ ($0.5 \leq x \leq 1.5$) for fields up to 14 kOe were traced, all exhibiting typical ferrimagnetic ordering. The saturation magnetization (M_s), obtained by extrapolating the M_s vs. $1/H$ plot to $1/H = 0$ for $H \geq 10$ kOe, increases as the x-values decrease. The magnetic moment values (in units of μ_B) obtained following the above-described methodology are presented in Table 1 (last column). More details regarding the methodology used to obtain the magnetic moment can be found in Franco Jr et al. [8]. Table 1 presents the cation distribution proposed for each synthesized $Mg_xFe_{3-x}O_4$ sample (center column, upper line), as a result of the combination of both Mössbauer and magnetization measurements. The Néel's approach ($\mu = \mu(B)-\mu(A)$) was used to calculate

the net magnetic moment associated to each sample regarding its particular cation distribution, with $\mu(B)$ and $\mu(A)$ representing the magnetic moments associated to sites B and A, respectively [16]. The calculated values of the magnetic moment per unit cell (μ), using the cation distribution provided by the Mössbauer and magnetization data, are listed in the fifth column of Table 1 (see upper line). In obtaining these results it was admitted that the cations' distribution was evenly spread throughout the nanoparticle. In addition, the effect of spin canting on the total magnetic moment of the nanoparticle was considered and found to be negligible. Results reported in the literature have shown an unusual magnetization enhancement in nanoscale mechano-synthesized $MgFe_2O_4$ [13,17]. It was found that the saturation magnetization of $MgFe_2O_4$ nanoparticles, with an average crystal-lite size of about 8.5 nm, reaches values of up to 50% more than that of bulk $MgFe_2O_4$. Also, it was verified that this enhanced magnetization decreases with increasing size of the nanoparticle [17]. According to the authors such behaviors are attributed to the nearly random distributions of magnetic cations on the nanopar-ticles' surface. To extend the discussion presented in Ref. [17] for the samples studied in this work ($\sim$45 nm) it was found that the increase in the saturation magnetization is less than 10%.

Room-temperature (300 K) Raman spectra of samples $Mg_xFe_{3-x}O_4$ ($x = 0.5$, 1.0, and 1.5) were recorded in the range of 180–850 cm^{-1}, as shown in Fig. 5. The Raman features indicated in Fig. 5 (dotted lines) are assigned to the vibrational modes from the nanoparticle's crystalline structure. Raman features other than those related to the spinel phase ($Mg_xFe_{3-x}O_4$) were not observed, as for instance from FeO, α-Fe_2O_3, or MgO. The assignments of the Raman modes took into account the fact that $MgFe_2O_4$ is an oxide with an inverse-like spinel structure, belonging to the space group $O_h^7(Fd\bar{3}m)$. Note that in this inverse structure half of the trivalent ions (Fe^{3+}) are located in tetrahedral (A) sites whereas the other half of the trivalent ions (Fe^{3+}) and all divalent ions (Mg^{2+}) are randomly distributed in octahedral (B) sites. The primitive unit cell of $MgFe_2O_4$ is rhombohedral, containing two A-sites, four B-sites, and eight oxygen ions. As a result, factor group analysis predicts the presence of five Raman modes (A_{1g}, E_g, and $3T_{2g}$), all of them observed in the present investigation. However, there is no consensus in the literature regarding the origin of the Raman vibrational modes in cubic ferrites. Some authors state that all observed Raman modes are related to the tetrahedral-like sublattice [18–20]. Others, in contrast, claim that cubic ferrites containing tetrahedral $Fe^{3+}O_4$ are characterized by a strong A_{1g} Raman band in the 660–720 cm^{-1} region, reflecting the local lattice effect in the tetrahedral sublattice, whereas the Raman modes observed in the lowest frequency region (460–640 cm^{-1}) are dominated by the stretching vibration associated to the octahedral $Fe^{3+}O_6$ sublattice [21]. Despite the previously mentioned disagreement all authors agree that the highest-frequency Raman modes are associated to the tetrahedral sublattice.

Although the factor group analysis predicts the presence of only five Raman modes our fitting procedure, using Lorentzian-like lines, reveals seven structures around 215, 335, 400, 480, 560, 670, and 715 cm^{-1} (see dotted lines in Fig. 5). In a recent study, while investigating the cubic ferrite $MgFe_3O_4$ Wang et al. [22] reported the presence of seven Raman modes peaking at energies very much close to the values we found in the present investigation. Those authors [22] stated that the modes located around 715 and 333 cm^{-1} have symmetries A_{1g} and E_g, respec-tively, whereas the Raman modes found around 217, 486, and 554 cm^{-1} have the $3T_{2g}$ symmetry. The Raman mode Wang et al. [22] found at 646 cm^{-1} was attributed to order–disorder effect. Indeed, no comment regarding the origin of the Raman mode found around 390 cm^{-1} was made by the authors [22].
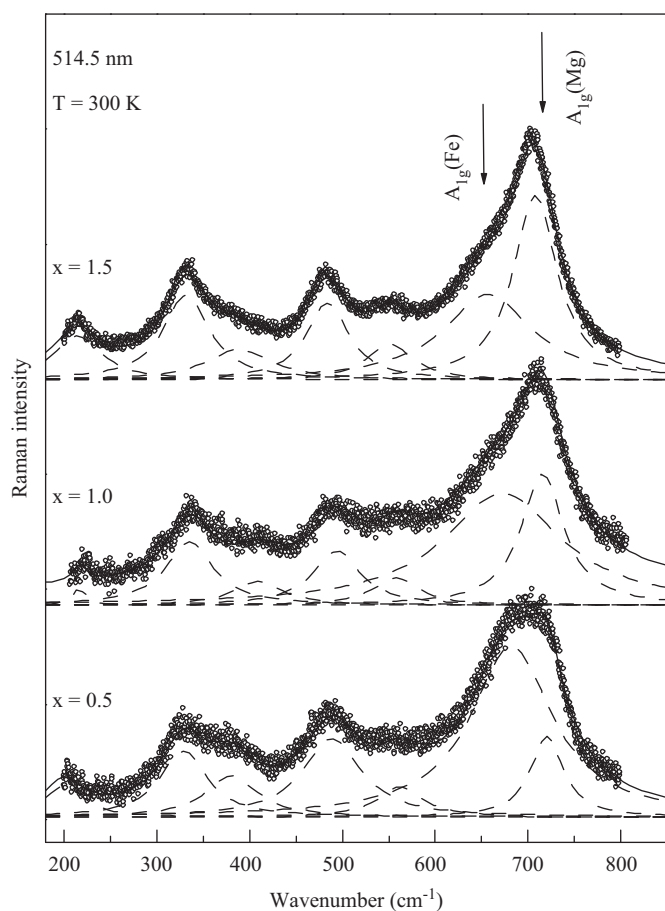
Fig. 5. Room-temperature Raman spectra of $Mg_xFe_{3-x}O_4$ samples ($x = 0.5$, 1.0, and 1.5) using the Ar^+ 514.5 nm laser line.

Differently from the proposal of Wang et al. [22] our data suggest that the Raman mode peaking at $670\,cm^{-1}$ is due to the substitution of the Fe ions by Mg ions in the tetrahedral sites and not associated to order–disorder effect. We claim that the large mass difference between the two ions (Fe^{3+} and Mg^{2+}) splits the A_{1g} mode into two branches; the lightest ion (Mg^{2+}) responds for the Raman mode peaking at $715\,cm^{-1}$ whereas the heaviest ion (Fe^{3+}) accounts for the presence of the Raman mode peaking at $670\,cm^{-1}$, as indicated in Fig. 5. Note from Fig. 5 that as the Mg-content (x) increases a gradual red shift of both Raman modes (670 and $715\,cm^{-1}$) is observed while the relative intensity between the two modes also changes. The variation of the integrated intensity of the Raman modes peaking at $670\,cm^{-1}$ (labeled A_{1g}(Fe)) and at $715\,cm^{-1}$ (labeled A_{1g}(Mg)), with respect to the total spectrum, as a function of the Mg-content is presented in Fig. 6. Note from Fig. 6 that the sum of the integrated intensity of both A_{1g} modes is approximately constant and about 50% of the total intensity of the Raman spectrum.

According to literature the A_{1g}(Fe) Raman mode is associated to the stretching vibrational mode of the tetrahedral $Fe-O_4-M_{12}^{1,2}$. Likewise, the A_{1g}(Mg) Raman mode is associated to the stretching vibrational mode of the tetrahedral $Mg-O_4-M_{12}^{1,2}$. Therefore, the integrated intensity of this Raman mode is proportional to the number of the corresponding oscillators. In other words, in the $Mg_xFe_{3-x}O_4$ samples the integrated intensity of the A_{1g}(Fe) Raman mode (I_{Fe}) is proportional to the Fe-content ($3-x$), whereas the integrated intensity of the A_{1g}(Mg) Raman mode (I_{Mg}) scales with the Mg-content (x). Therefore, the integrated intensity of the A_{1g}(Fe) Raman mode decreases as the Mg-content increases. The

inverse trend should be observed for the A_{1g}(Mg) Raman mode. Taking the above discussion into consideration one can obtain the Mg-content in the tetrahedral (A) site from the Raman data (x^A_{Raman}) as follows:

$$x^A_{Raman}(Mg) = \frac{I_{Mg}}{2(I_{Mg} + RI_{Fe})}. \tag{2}$$

In Eq. (2) R represents the relative oscillator strength of the $Mg-O_4-[(12-n)Fe+nMg]$ bonds with respect to the $Fe-O_4-[(12-n)Fe+nMg]$ bonds, where n is the number of bounded Mg ions. Likewise, from the Mössbauer data, a similar $x^A_{Mössbauer}(Mg)$ parameter can be introduced and the values obtained from the curve fitting of the Mössbauer spectra, from which we can extract the values of Fe-content associated with the sublattice A and, consequently, the Mg-content values in this sublattice (see third column of the Table 1). The calculated values of $x^A_{Raman}(Mg)$ (see Eq. (2)) versus the calculated values of $x^A_{Mössbauer}(Mg)$ are plotted in Fig. 7. A satisfactory agreement between the Mg-content in the A-site, as obtained by Raman
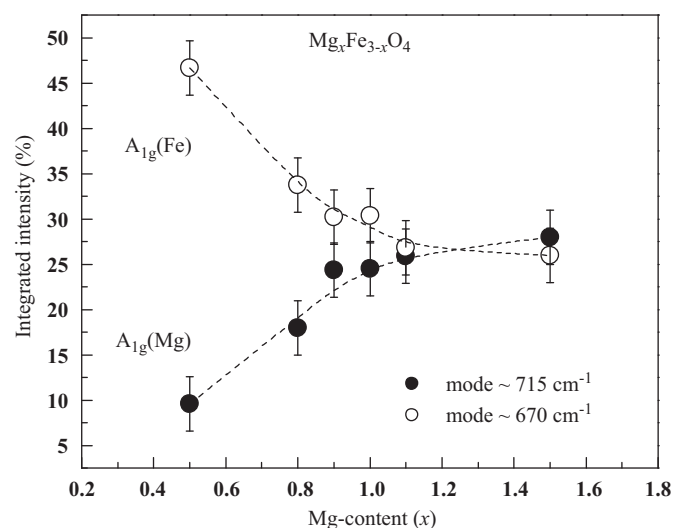

Fig. 6. Integrated intensity (%) of the A_{1g}(Fe) and A_{1g}(Mg) Raman modes as a function of the Mg-content.
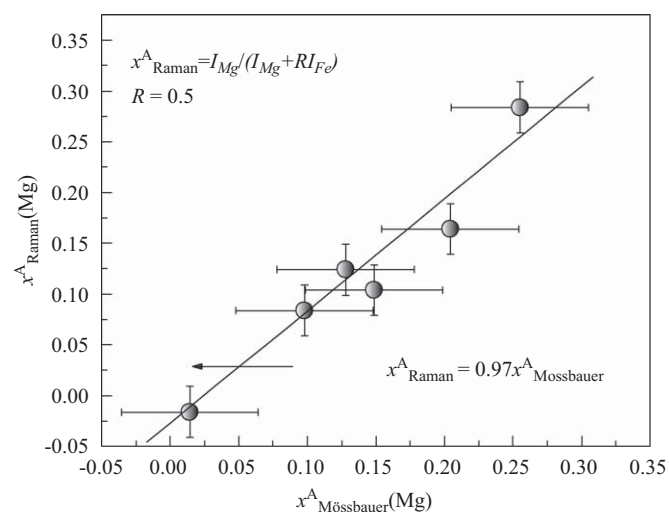

Fig. 7. Mg-content (x^A_{Raman}) calculated using Eq. (2) versus the Mg-content obtained from the Mössbauer ($x^A_{Mössbauer}$) data. The solid line represents the linear fit: $x^A_{Raman} = 0.97x^A_{Mössbauer}$.

and Mössbauer measurements, was obtained using $R = 0.5$. Unfortunately, R-values are not available in the literature for comparison.

Finally, the ion content (Fe and Mg) associated to the A-site, as obtained by Raman, plus charge balance requirements allowed the determination of the total cation distribution of all samples, as shown in Table 1 (third column, lower row). Note from the data displayed in Table 1 that the cation distributions obtained by both Mössbauer and Raman spectroscopies agree quite well. Further, the calculated magnetic moment associated to each cation distribution is in good agreement with the magnetic moment obtained experimentally. Observe also in Table 1 that, for samples with $x = 1.1$ and 1.5, the charge balance required for the cations' distribution imposed the presence of oxygen vacancy [23,24].

The monotonic red shifts observed in the Raman frequencies of $A_{1g}(Mg)$ and $A_{1g}(Fe)$ modes ($Mg_xFe_{3-x}O_4$ samples) as a function of x are shown in Figs. 8(a) and (b), respectively. Similar red shifts were also observed for the E_{1g} Raman modes (450–550 cm^{-1}). This finding can be explained considering alloy effects, which predict a shift in the Raman frequency with the introduction of a third ion at different amounts [25]. Further, the Raman frequency indirectly accounts for the population of substitutional Mg, so that the higher the number of Mg ions bound in the Fe(Mg)–O$_4$–[(12−n)Fe+nMg] bonds, where n is the number of

Mg ion bonds, the smaller the Raman frequency. In addition, it should also be mentioned that the radius of Fe^{3+} and Mg^{2+} ions in the tetrahedral sites are 0.63 and 0.71 Å, respectively. Then, substitution of Fe^{3+} by Mg^{2+} makes the tetrahedral site larger and consequently decreases the frequency of the vibrational modes.

4. Conclusion

The influence of Mg-content on the cation (Fe^{3+} and Mg^{2+}) distribution in the $Mg_xFe_{3-x}O_4$ ($0.5 \leq x \leq 1.5$) system was investigated using Raman and Mössbauer spectroscopies. As far as the cation distribution among the two available sites is concerned we found that this material system ($Mg_xFe_{3-x}O_4$) presents a mixed-like spinel structure at lower x-values, shifting towards an inverse-like spinel structure as the Mg-content increases. Due to the large mass difference between iron and magnesium ions the A_{1g} Raman mode splits into two branches, allowing us to quantify the Fe^{3+} and Mg^{2+} distribution in the tetrahedral sites and, consequently, to obtain the cation distribution for the $Mg_xFe_{3-x}O_4$ ($0.5 \leq x \leq 1.5$) system. The cation (Fe^{3+} and Mg^{2+}) distribution for the $Mg_xFe_{3-x}O_4$ ($0.5 \leq x \leq 1.5$) system was also obtained from the combination of Mössbauer and magnetization data. We found that the cation distribution obtained by Raman spectroscopy agrees quite well with the cation distribution obtained by Mössbauer and magnetization data. We found the $A_{1g}(Fe)$ and $A_{1g}(Mg)$ Raman modes shifting towards low frequencies as the Mg-content increases in the range $0.5 \leq x \leq 1.5$. This finding was attributed to changes in cation distribution as the x-value increases, once substitution of Fe^{3+} by Mg^{2+} makes the tetrahedral site larger and consequently reduces the frequency of the vibrational modes.

Acknowledgments

References

[1] J.G. Lee, J.Y. Park, Y.J. Oh, C.S. Kim, J. Appl. Phys. 84 (1998) 2801–2804.
[2] L.G.J. De Haart, A.J. De Vries, G. Blasse, Mater. Chem. Phys. 13 (1985) 85–90.
[3] M.H. Khedr, M. Bahgat, W.M.A. El Rouby, Mater. Technol. 23 (2008) 27–32.
[4] Y. Shimizu, H. Arai, T. Seiyama, Sensors Actuators 7 (1985) 11–22.
[5] R.K. Kotnala, J. Shah, B. Singh, H. Kishan, S. Singh, S.K. Dhawan, A. Sengupta, Sensors Actuators B Chem. 129 (2008) 909–914.
[6] B.L. Yang, D.S. Cheng, S.B. Lee, Appl. Catal. 70 (1991) 161–173.
[7] M.J. Seong, M.C. Hanna, A. Mascarenhas, Appl. Phys. Lett. 79 (2001) 3974–3976.
[8] A. Franco Jr, T.E.A. Pereira, E.C.O. Lima, E.S. Nunes, V. Zapf, Appl. Phys. A Mater. Sci. Process. 94 (2009) 131–137.
[9] B.D. Cullity, Elements of X-ray Diffraction, Addison-Wesley, Reading, MA, USA, 1978.
[10] E.E. Sileo, L.G. Rodenas, C.O. Paiva-Santos, P.W. Stephens, P.J. Morando, M.A. Blesa, J. Solid State Chem. 179 (2006) 2237–2244.
[11] D.C. Kahn, M. Misra, A.R. Das, J. Appl. Phys. 53 (1982) 2722–2724.
[12] A.A. Pandit, S.S. More, R.G. Dorik, K.M. Jadhav, Bull. Mater. Sci. 26 (2003) 517–521.
[13] V. Sepelák, A. Feldhoff, P. Heitjans, F. Krumeich, D. Menzel, F.J. Litterst, I. Bergmann, K.D. Becker, Chem. Mater. 18 (2006) 3057–3067.
[14] F. Nakagomi, S.W. da Silva, V.K. Garg, A.C. Oliveira, P.C. Morais, A. Franco Jr, E.C.D. Lima, J. Appl. Phys. 101 (2007) 09M514.
[15] G.A. Sawatzlky, F. Van Der Woude, A.H. Morrish, Phys. Rev. 187 (1969) 747–757.
[16] M.A.G. Soler, E.C.D. Lima, S.W. da Silva, T.F.O. Melo, A.C.M. Pimenta, J.P. Sinnecker, R.B. Azevedo, V.K. Garg, A.C. Oliveira, M.A. Novak, P.C. Morais, Langmuir 23 (2007) 9611–9617.
[17] V. Sepelák, I. Bergmann, D. Menzel, A. Feldhoff, P. Heitjans, F.J. Litterst, K.D. Becker, J. Magn. Magn. Mater. 316 (2007) e764–e767.
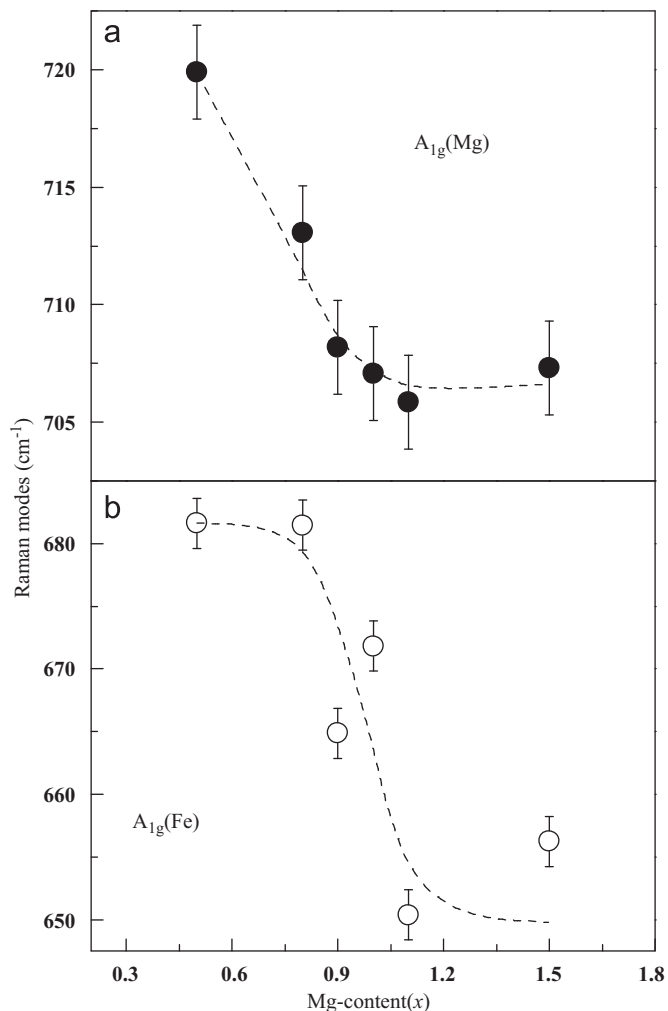[18] W.B. White, B.A. DeAngelis, Spectrochim. Acta A Mol. Spectrosc. 23 (1967) 985–995.

Fig. 8. Magnesium-content dependence of the Raman mode frequency for (a) $A_{1g}(Mg)$ and (b) $A_{1g}(Fe)$ in the $Mg_xFe_{3-x}O_4$ ($0.5 \leq x \leq 1.5$) system.

[19] J.L. Verble, Phys. Rev. B 9 (1974) 5236–5248.
[20] O.N. Shebanova, P. Lazor, J. Solid State Chem. 174 (2003) 424–430.
[21] J. Kreisel, G. Lucazeau, H. Vincent, J. Solid State Chem. 137 (1998) 127–137.
[22] Z. Wang, P. Lazor, S.K. Saxena, Hugh St C. O'Neill, Mater. Res. Bull. 37 (2002) 1589–1602.

[23] R.A. Candeia, M.A.F. Souza, M.I.B. Bernardi, S.C. Maestrelli, I.M.G. Santos, A.G. Souza, E. Longo, Mater. Res. Bull. 41 (2006) 183–190.
[24] Yujie Huang, Yan Tang, Jun Wang, Qianwang Chen, Mater. Chem. Phys. 97 (2006) 394–397.
[25] Y.A. Pusep, S.W. da Silva, J.C. Galzerani, A.G. Milekhin, V.V. Preobrazhenskii, B.R. Semyagin, I.I. Marahovka, Phys. Rev. B 52 (1995) 2610–2618.